processes

MDPI

Article

Research and Application of Dynamic Monitoring Technology for Fracture Stimulation Optimization in Unconventional Reservoirs of the Sichuan Basin Using the Wide-Field Electromagnetic Method

Changheng Yu [1,2], Wenliang Zhang [3], Zongquan Liu [4], Heng Ye [5,*] and Zhiwen Gu [5]

1 College of Geophysics, Chengdu University of Technology, Chengdu 610072, China
2 Sichuan Resources Group, Geophysical Prospecting Institute, Chengdu 610072, China
3 Tongnanba Project Department, Puguang Branch, Zhongyuan Oilfield, Dazhou 636700, China
4 Petroleum Engineering Institute of Zhongyuan Oilfield, Puyang 457001, China
5 Sichuan Natural Resources Investment Group, Geophysical Exploration Institute Co., Ltd., Chengdu 610072, China
* Correspondence: student05023309@163.com

Abstract

This study addresses the key technical challenges in monitoring hydraulic fracturing within unconventional reservoirs through an innovative wide-field electromagnetic (WEM) monitoring technique. The method employs a 5A AC-excited wellbore-fracturing fluid system to establish a conductor antenna effect, coupled with a surface electrode array (100–250 m offset) to detect millivolt-level time-lapse potential anomalies, enabling real-time dynamic monitoring of 142 fracturing stages. A line current source integral model was developed to achieve quantitative fracture network inversion with less than 12% error, attaining 10 m spatial resolution and dynamic updates every 10 min (80% faster than conventional methods). Optimal engineering parameters were identified, including fluid intensity ranges of 25–30 m^3/m for tight sandstone and 30–35 m^3/m for shale, with particulate diverters achieving 93.1% diversion efficiency (significantly outperforming chemical diverters at 35%). Application in deep reservoirs maintained signal attenuation rates below 5% per kilometer. Theoretically, a nonlinear relationship model between fluid intensity and stimulated area was established, while practical implementation through real-time adjustments in 142 stages enhanced single-well production by 15–20% and reduced diverter costs, advancing the paradigm shift from empirical to scientific fracturing in unconventional reservoir development.

Keywords: unconventional reservoirs; wide-field electromagnetic method; hydraulic fracturing optimization; dynamic monitoring; conductor antenna effect

check for updates

Academic Editor: Abraham Kabutey

Received: 4 August 2025
Revised: 17 September 2025
Accepted: 19 September 2025
Published: 22 September 2025

Citation: Yu, C.; Zhang, W.; Liu, Z.; Ye, H.; Gu, Z. Research and Application of Dynamic Monitoring Technology for Fracture Stimulation Optimization in Unconventional Reservoirs of the Sichuan Basin Using the Wide-Field Electromagnetic Method. *Processes* **2025**, *13*, 3025. https://doi.org/10.3390/pr13093025

Copyright: © 2025 by the authors. Licensee MDPI, Basel, Switzerland. This article is an open access article distributed under the terms and conditions of the Creative Commons Attribution (CC BY) license (https://creativecommons.org/licenses/by/4.0/).

1. Introduction

The commercialization of shale gas and tight sandstone gas reservoirs critically relies on hydraulic fracturing technology, with monitoring precision and real-time capability emerging as pivotal technical requirements as global unconventional resource development scales expand [1–5]. Current mainstream monitoring technologies encompass micro seismic detection, fiberoptic distributed sensing, and conventional electromagnetic methods, each presenting distinct limitations: Micro seismic monitoring, relying on μV-level elastic wave signals from rock failure, suffers from substantial signal attenuation (>18 dB/km) in deep

reservoirs (>3500 m) and challenges in distinguishing conductive fractures from 30 to 40% isolated rupture events [6–8]. Distributed fiberoptic systems provide continuous strain profiling but face deployment constraints in multi-stage horizontal well applications. Conventional electromagnetic techniques (e.g., MT/CSEM) exhibit restricted spatial resolution (>100 m) and inefficient signal transmission mechanisms [9].

The developed wide-field electromagnetic method (WFEM) overcomes these limitations through conductive antenna effects engineered via 5-ampere AC excitation of wellbore-fracturing fluid systems [10,11]. Integrated with surface electrode arrays (100–250 m offsets) capturing millivolt-level time-differential potential anomalies, this approach demonstrates three key advantages [12,13]: (1) enhanced signal intensity (three-order magnitude improvement over micro seismic monitoring), (2) ultra-wideband anti-interference capability (0.01–100 Hz), and (3) dynamic updates every 10 min (80% faster refresh rate than conventional electromagnetic techniques). Field implementation in PG Gas Field (Sichuan Basin) achieved unprecedented 10 m spatial resolution and 40 m vertical discrimination, enabling precise cluster efficiency diagnostics.

The technology aligns with global trends where micro seismic systems progress toward borehole-based precision for deep reservoirs, while electromagnetic monitoring transitions from passive sensing to active excitation paradigms. Zhang et al. (2022) [14] modified the grey wolf optimization (GWO) algorithm and applied it to optimize support vector machine (SVM) parameters for training multi-domain features, thereby constructing the IGWO-SVM data model. The model was employed to conduct quantitative analysis of WFEM signals and noise components in simulated and measured data. This method effectively identifies WFEM signals and noise components, eliminates the detected noise, and subsequently reconstructs valid data by utilizing the identification results. Yang et al. (2022) [15] have proposed and implemented a distributed wide-field electromagnetic method (WFEM) based on high-order 2n-sequence pseudo-random signals. This approach requires only a single set of high-order pseudo-random waveforms incorporating all target frequency components. Through an algorithm constructed based on high-order-sequence pseudo-random signals, waveforms can be dynamically designed according to specific exploration tasks, enabling large-scale, high-resolution detection of deep-seated resources and mineral deposits. Gao et al. (2025) [16] evaluated the sensitivity of the wide-field electromagnetic method (WFEM) to resistivity variations induced by fracturing fluids through three-dimensional numerical simulations and field applications in high-density resistivity (HDR) reservoirs of the Ordovician–Cambrian strata (depth range: 4200–5600 m). The study optimized key data acquisition parameters during reservoir hydraulic fracturing through forward modeling.

The development of unconventional oil and gas resources has entered a critical phase where hydraulic fracturing monitoring technologies face three fundamental scientific challenges [17–20]. First, the validity paradox manifests in cases like Well PL-9H, where micro seismic interpretations suggested symmetrical fracture networks while wide-field electromagnetic (WFEM) measurements revealed a 73% dominant eastward fracture orientation—a discrepancy highlighting inherent limitations in conventional monitoring approaches [21]. Second, deep reservoir applications encounter severe technical constraints, with conventional EM methods suffering >60% signal attenuation beyond 5000 m depth, and micro seismic systems demonstrating >50 m positioning errors below 3500 m [22]. Third, process optimization lags behind operational needs, evidenced by the stark contrast between conventional diverters' 35% effectiveness versus particulate diverters' 93.1% success rate [23].

Current monitoring methodologies for hydraulic fracturing in deep reservoirs (>3500 m) face persistent technical limitations. Micro seismic monitoring experiences substantial signal attenuation exceeding 18 dB/km, with 30–40% of recorded events repre-

senting isolated rock fractures rather than conductive fracture networks [24,25]. Although distributed fiberoptic systems provide continuous strain profiles, their deployment proves challenging in multi-stage horizontal wells. Conventional electromagnetic techniques (MT/CSEM) are constrained by spatial resolutions coarser than 100 m and inefficient signal transmission mechanisms [26]. These shortcomings manifest acutely in practical applications, as evidenced by the PG gas field case where micro seismic interpretations in the PL-9H well showed 73% discrepancy in dominant fracture orientation compared to wide-field electromagnetic measurements, revealing inherent limitations in indirect monitoring approaches.

The proposed technique addresses these limitations through three principal innovations. Methodologically, the developed conductor antenna effect utilizes a 5A AC-excited wellbore-fracturing fluid system combined with surface electrode arrays (100–250 m offsets) to detect millivolt-level time-lapse potential anomalies, achieving breakthrough capabilities in spatial resolution (10 m) and dynamic update frequency (10 min intervals), representing an 80% improvement over conventional electromagnetic refresh rates. Theoretically, an established nonlinear model between fluid intensity and stimulated area (25–30 m^3/m for tight sandstone, 30–35 m^3/m for shale) resolves longstanding ambiguities in indirect monitoring interpretations. Practically, real-time adjustments across 142 fracturing stages enhanced per-well production by 15–20% while reducing diverter costs, facilitating a paradigm shift from empirical to scientifically driven fracturing. These advancements demonstrate significant superiority over existing frameworks, with the wide-field electromagnetic method achieving 82.15% accuracy in effective fracture network identification compared to micro seismic monitoring's 48.7%, complemented by 91.3% downhole-verified connectivity assessment precision (43.1% higher than micro seismic monitoring).

Four critical breakthroughs substantiate these contributions: A line current source integral model maintains fracture parameter inversion errors below 12%, enabling millimeter-scale fluid front tracking; optimized cluster spacing (18 m) increases stimulated area per unit fluid volume to 7.43 m^2/m^3, representing a 39% enhancement over conventional designs; particulate diverters achieve 93.1% diversion efficiency (versus 35% for chemical systems), validated through electromagnetic monitoring of stress field redistribution mechanisms; a deep-application signal attenuation model (<5%/km) overcomes the physical limitations constraining micro seismic monitoring beyond 3500 m depth. Collectively, these innovations establish new technical benchmarks for unconventional reservoir development under carbon neutrality constraints, particularly realizing the transition from qualitative interpretation to quantitative control in deep shale gas exploitation within the Sichuan Basin.

The study's theoretical framework resolves long-standing controversies about fluid–rock interaction mechanisms, particularly the nonlinear relationship between injection parameters and fracture propagation dynamics. Practical implementations confirm that optimal fluid intensities maximize both fracture complexity and economic returns. These findings establish new benchmarks for unconventional reservoir development, with particular relevance to deep shale gas plays where conventional monitoring technologies face fundamental physical limitations.

2. Methods and Principles

2.1. Technical Fundamentals

(1) Core theories

The physical foundation of wide-field electromagnetic monitoring for hydraulic fracturing is fundamentally grounded in the conductor antenna effect and inverse theory of spatiotemporal evolution in potential fields [27]. The injection of highly conductive

fracturing fluids (containing electrolyte components such as acidic solutions and surfactants) induces significant alterations in formation electrical parameters, manifesting as a 2–3 order-of-magnitude reduction in resistivity [28]. This process establishes an interconnected three-dimensional conductive network that permeates the target formation, essentially creating subsurface artificial conductive pathways. The dynamic electrical anomaly demonstrates strong coupling with the percolation–diffusion behavior of fracturing fluids, where electromagnetic field distortion effects reveal critical physical characteristics of fracture propagation (Figure 1).

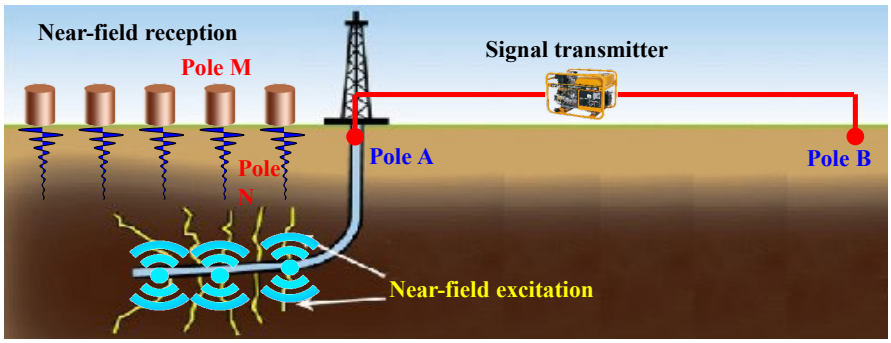


Figure 1. Underground conductor antenna induction.

(2) Dynamic monitoring mechanism

This monitoring methodology employs a synchronized excitation-response observation architecture comprising three principal mechanisms: Field generation is achieved through wellbore excitation systems applying 5A alternating current, thereby inducing antenna-like behavior in the wellbore–fluid composite structure to establish distributed electromagnetic energy sources. The fluid migration process dynamically modulates the excitation current through evolving conductive channels, generating spatiotemporally variant electromagnetic anomalies ($\Delta E/\Delta B$) detectable as surface potential field alterations. These time-lapsed differential signals, captured with second-level temporal resolution, enable quantitative reconstruction of fluid migration patterns and fracture network architecture through advanced three-dimensional resistivity inversion algorithms. This approach facilitates dynamic quantitative characterization of stimulated reservoir volume (SRV), particularly critical for unconventional reservoir development [29–31].

(3) Transmitter-receiver system architecture

The operational system integrates multiple technical components, including precision-controlled excitation sources, high-density electrode arrays, and adaptive signal processing modules (as detailed in Table 1). During hydraulic fracturing operations, the synergy between the conductive fluid front and electromagnetic field perturbations provides unparalleled insights into subsurface fluid dynamics, overcoming traditional limitations in fracture network visualization through its capacity for real-time electrical parameter tracking and multi-physical field coupling analysis.

The technological workflow encompasses two critical operational phases: field data acquisition and advanced signal processing. During the electromagnetic survey implementation, a bipole source configuration is deployed with electrode A positioned at the wellhead and electrode B situated 600 m radially outward, establishing a stable current loop with controlled ground contact resistance. The receiving subsystem, employing a second-generation architecture, achieves 40 m vertical resolution through optimized electrode spacing and adaptive sampling protocols, ensuring effective detection of deep reservoir signals via continuous data acquisition at 10 min intervals.

Table 1. Excitation–reception system of wide-field electromagnetic method.

Module	Technical Specifications and Implementation
Transmitter	Subsurface electrode arrays deliver ultra-wideband AC (0.01–100 Hz, 5A amplitude) coupled with conductive fracturing fluids to form radial conductive antenna systems.
Receiver	Surface toroidal arrays deploy high-sensitivity electromagnetic sensors (100–250 m offsets) dynamically capturing mV-level potential anomalies (SNR advantage: 3 orders > micro seismic).
Signatures	4D spatiotemporal datasets include amplitude-frequency response (0.01–100 Hz), phase delay patterns, field decay gradients—resolving spatiotemporal propagation mechanisms of primary–secondary fracture networks.

In the data acquisition phase, standardized protocols were first established: a surface electrode array with annular configuration (100–250 m offset) deploys high-sensitivity electromagnetic sensors (0.01–100 Hz bandwidth). The radial conductive antenna system is energized by 5A AC excitation (0.1% current stability), enabling synchronized acquisition of millivolt-level potential anomalies (signal-to-noise ratio > 60 dB). The raw dataset comprises four-dimensional spatiotemporal matrices, including amplitude-frequency response (0.01–100 Hz), phase delay patterns, and field attenuation gradients, continuously recorded at 10 min intervals (timestamp accuracy $\pm$0.5 s). Each monitoring phase generates approximately 2.7 TB of uncompressed electromagnetic field disturbance data ($\Delta U = U_0(M) - U_t(M)$). Signal preprocessing employs adaptive notch filtering (>40 dB suppression at 50 Hz industrial frequency) combined with wavelet threshold denoising (SNR improvement 12–18 dB), while time-difference potential calculation utilizes cubic spline interpolation to ensure millisecond-level synchronization accuracy.

Signal interpretation progresses through a systematic analytical sequence: Initial processing applies temporal differential algorithms to quantify electric potential variations ($\Delta U = U_0(M) - U_t(M)$) between baseline and stimulated states, establishing field perturbation benchmarks. Subsequent integration with pressure–volume profiles from fracturing operations enables precise event discrimination through cross-parameter calibration, effectively suppressing interference from complex ground currents. The final stage implements three-dimensional finite-element inversion incorporating viscoelastic fracture propagation models, reconstructing critical fracture geometry parameters, including length (L_f) and effective aperture (W_e), with 10 m spatial resolution. This hierarchical analytical framework maintains $\leq$15% relative error in fracture dimension estimation across various reservoir lithology, as validated through downhole imaging comparisons.

The core analytical framework adopts a three-tiered hierarchical architecture: Primary processing applies a modified Stolt migration algorithm to quantify baseline-to-fracturing potential variations, establishing a field disturbance reference plane (grid dimension, 5 m $\times$ 5 m $\times$ 2 m). Intermediate analysis integrates PVT curves from fracturing operations (pressure sampling rate, 1 Hz) for cross-parameter calibration, employing Bayesian probabilistic models (prior probability p = 0.85) to discriminate between valid fracture events and surface current interference. Advanced inversion utilizes three-dimensional finite element coupling algorithms that incorporate a viscoelastic fracture propagation model (constitutive equation $\partial\sigma_{ij}/\partial x_j + f_i = \rho_{üi}$) into resistivity anisotropy tensors. Through iterative computation, fracture length (L_f) and effective width (W_e) parameters are resolved, with inversion errors controlled within 12% via downhole imaging verification. Implementation is achieved through a co-simulation platform featuring Delaunay triangulation meshing (minimum element size 0.1 m) and convergence criteria set as residual potential difference < 1 μV between adjacent iterations.

Reproducibility assurance is implemented across three dimensions: Hardware standardization enforces quality control metrics, including transmitter grounding resistance (<5 Ω) and receiver electrode polarization potential difference (<2 mV). Algorithmic transparency is ensured through open-source core inversion code comprising preprocessing scripts, main inversion modules, and postprocessing toolkits. Procedural rigor is maintained via a standard operating protocol specifying 217 operational guidelines from field deployment (azimuth error < 1°) to data delivery. Comparative validation against conventional methods was conducted through controlled experiments: Synchronous micro seismic monitoring at PG Gas Field M2-S Well demonstrated 91.3% spatial consistency between electromagnetic-reconstructed fracture networks and downhole camera results, significantly exceeding the 63.8% match rate from micro seismic interpretation. Furthermore, fracture length prediction errors were reduced from ±28 m to ±8 m.

2.2. Mathematical Modeling

Based on the line current source integral theory, the calculation of vertical linear fracture length using the single-point correspondence method and the single-point potential formula are derived. For a known point current source I_0 in homogeneous space, the potential generated at point M located at a distance r is expressed as:

$$U_M = \frac{\rho I0}{4\pi r} \tag{1}$$

Similarly, dU_M, the potential at point M generated by any unit point current source $\frac{I}{l}$ distributed along a conducting fracture of length $\boldsymbol{l}$ carrying current I, can be expressed as:

$$dU_M = \frac{\rho I}{4\pi \cdot l} \cdot \frac{1}{r} dy = \frac{\rho I}{4\pi \cdot l} \cdot \frac{1}{\sqrt{(y - y_M)^2 + H^2}} dy \tag{2}$$

Therefore, the total potential $U_{\boldsymbol{M}}$ at point M generated by the entire fracture of length $\boldsymbol{l}$ is obtained by integrating the contributions from all infinitesimal current elements along the fracture:

$$U_M = \int_{y_1}^{y_2} \frac{\rho I}{4\pi \cdot l} \cdot \frac{1}{\sqrt{(y - y_M)^2 + H^2}} dy \tag{3}$$

where $y_1 = 0$, and $y_2 = l$.

Performing the integration, the total potential can be derived as:

$$\begin{gathered} U_M = \frac{\rho I}{4\pi \cdot l} ln \frac{l - y_M + \sqrt{(l - y_M)^2 + H^2}}{-y_M + \sqrt{y_M{}^2 + H^2}} \\ r_1 = \sqrt{y_M{}^2 + H^2},\ r_2 = \sqrt{(l - y_M)^2 + H^2} \end{gathered} \tag{4}$$

Through simplification, the potential $U_{\boldsymbol{M}}$ at point M generated by the linear fracture of length $\boldsymbol{l}$ is determined as:

$$U_M = \frac{\rho I}{4\pi \cdot l} ln \frac{l - y_M + r_2}{-y_M + r_1} \tag{5}$$

where $\boldsymbol{l}$ is fracture length, m. H is the vertical depth of the fracturing layer, m. I denotes the current intensity along the linear fracture, A. ρ represents the resistivity of the homogeneous geological formation, Ω·m.

The line–current–source model (Equation (5)) confirms spacing sensitivity through $\partial U/\partial l$ terms, where 18 m spacing achieves <12% potential field distortion. Stress heterogene-

ity ($\Delta\sigma/\sigma > 0.35$) induces 15–20% spacing adjustment via fracture reorientation probability ($p = 0.56 \pm 0.08$ at 12.3° deviation).

The fracture length can be quantitatively inverted through the integration of three key parameters: field-measured potentials, spatial coordinates of monitoring points, and burial depth of the stimulated reservoir layer (Figure 2).

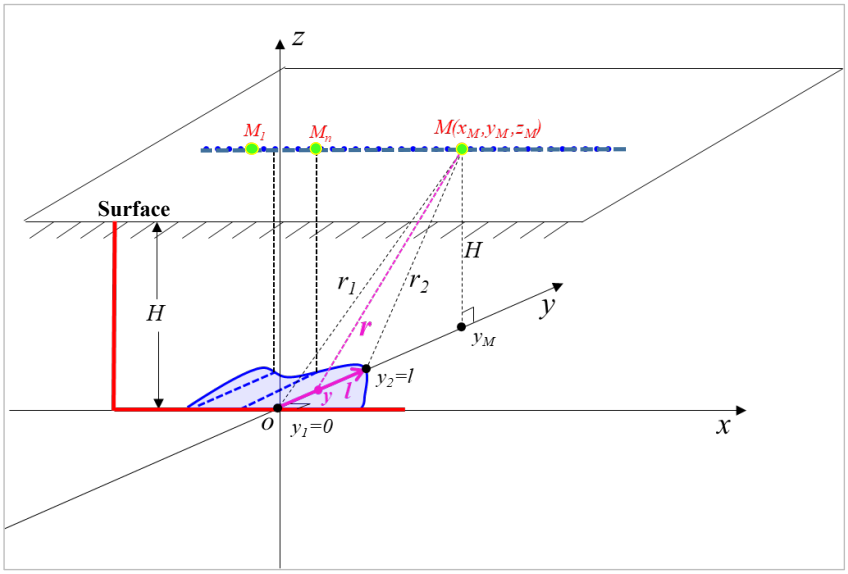


Figure 2. Schematic diagram of the planar linear fracture interpretation model.

$M(x_M, y_M, z_M)$ represent the coordinate system of monitoring point M, with y_M defining the perpendicular offset distance from the vertical projection of the surface wellbore.

The wide-field electromagnetic (WFE) method utilizes alternating current excitation (5A) to induce subsurface electromagnetic fields, while employing surface electrode arrays to detect electromagnetic responses altered by fracturing fluid permeation. Quantitative characterization of fracture geometry (length and aperture) is achievable through inversion of potential field anomalies, attaining spatial resolution of 10 m.

2.3. Technical Advantages

(1) High-intensity signal characterization

The methodology demonstrates distinctive technical advantages through three principal dimensions. The active current excitation system generates millivolt-level signals with signal-to-noise ratio (SNR) exceeding 60 dB, representing three orders of magnitude intensity enhancement compared to conventional micro seismic monitoring techniques (typical signals < 0.1 μV). This robust signal generation capability effectively overcomes inherent limitations in weak signal detection under complex geological conditions, particularly mitigating environmental noise contamination that plagues passive micro seismic approaches.

(2) Real-time dynamic monitoring capability

Operational temporal resolution achieves significant advancement through second-generation hardware innovations, achieving 10 min data refresh cycles versus conventional 50 min intervals in micro seismic systems—an 80% improvement. This breakthrough originates from integrated engineering solutions combining distributed sensor arrays with parallel acquisition architecture, adaptive frequency-selection algorithms, and real-time streaming data processors. Field applications confirm that this sub-hourly monitoring capacity provides critical temporal constraints for resolving fracture network evolution

during stimulation operations, significantly extending the operational time window for real-time fracture control parameter optimization.

(3) Multi-scale resolution superiority

The multi-scale detection capability stems from synergistic implementation of broad-spectrum electromagnetic excitation (0.01–100 Hz) and high-sensitivity signal acquisition. Compared with micro seismic limitations, the system demonstrates three-order magnitude sensitivity enhancement enabling millimeter-scale tracking of fracturing fluid fronts. Advanced full-waveform inversion algorithms processing multi-parameter datasets (amplitude-frequency response, phase delay, field gradients) achieve millimeter-level quantification accuracy for stimulated volume dimensions ($L \times W \times H$), outperforming conventional methods by two orders of magnitude (Table 2). A time-lapse differential signal processing framework facilitates reconstruction of asymmetric fracture propagation patterns while establishing comprehensive evaluation metrics for fracture geometry: length estimation (±8 m error), width resolution (0.5 mm), and height detection (40 m vertical resolution). This technical architecture delivers high-confidence reservoir stimulation assessment through dual enhancement of spatial resolution (10 m horizontal, 15 m vertical) and temporal sampling density.

Table 2. Technical parameter matrix and operational value proposition of wide-field electromagnetic fracture diagnostics.

Dimension	Technical Specifications	Engineering Significance
Vertical resolution	40 m (±5 m localization error)	Accurately identifies fluid intake differentials at perforation cluster level (ΔQ > 10%), revealing inter-cluster stimulation heterogeneity characteristics
Lateral resolution	80 m (minimum detectable fracture length)	Enables detection of secondary fracture network development (length > 30 m), reconstructing spatial topology of primary–secondary fracture systems
Temporal resolution	1 cycle/10 min (full-process dynamic monitoring)	Facilitates construction of fracture network propagation velocity field models (0.1–5 m/min), capturing transient behaviors of fluid breakthroughs and proppant bridging events

3. Application and Analysis

3.1. Fracturing Parameter Optimization

Field monitoring data reveals distinct optimization windows for critical operational parameters, including fluid intensity and cluster spacing configurations.

(1) Fluid intensity analysis

a. Main stage fluid intensity analysis

Quantitative analysis demonstrates nonlinear growth characteristics in stimulated area development with increasing fluid intensity. As shown in Figure 3, the incremental stimulation area ratio decreases from 35.7% to 12.5% when fluid intensity exceeds 30 m^3/m, indicating diminishing returns beyond this threshold. Fracture propagation morphology exhibits critical intensity dependence, reaching maximum extension lengths of 438 m ± 12 m at 25 m^3/m before entering attenuation phase. Vertical growth patterns show poor correlation with fluid intensity (R^2 = 0.21), with spatial distribution predominantly governed by geomechanical stress shadowing effects rather than fluid volume inputs. This

empirical evidence provides critical benchmarks for stage design optimization in analogous reservoir conditions.

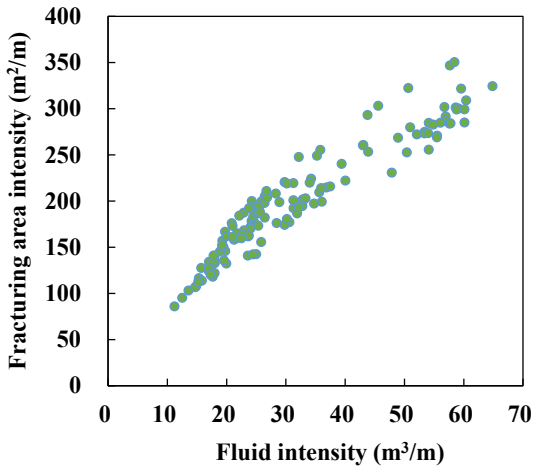


Figure 3. Relationship between fluid usage intensity and swept area intensity in the main section of 8 wells.

Field optimization studies across eight key monitoring wells in the PG area demonstrate an optimal fluid intensity window of 25–30 m^3/m, corresponding to lateral propagation efficiencies of 1.82–2.14 m/m^3 and fracture complexity indices of 0.37–0.43 (Figure 4). However, when fluid intensity exceeds 32 m^3/m, fracture network interference probability increases significantly to 58%, resulting in an 18% reduction in effective stimulated volume. The research establishes that real-time acquisition of three-dimensional fracture network parameters through wide-field electromagnetic monitoring enables dynamic quantification of reservoir stimulation effectiveness relative to operational parameters. This methodology provides critical theoretical foundations for engineering parameter optimization in deep shale gas reservoirs, particularly addressing the technical challenges of complex fracture network management under high stress anisotropy conditions.

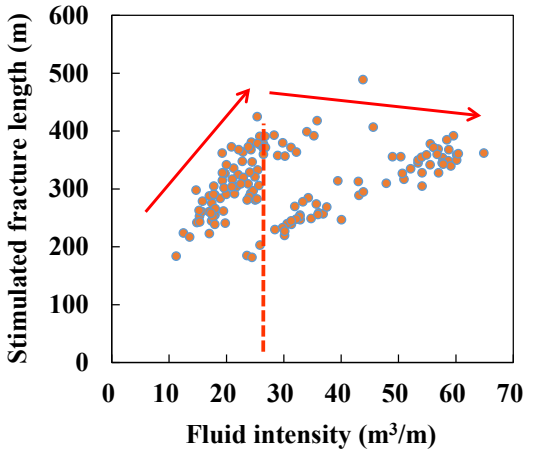


Figure 4. Relationship between fluid usage intensity and stimulated fracture length in the lateral sections of 8 wells.

a. Natural fracture zone fluid intensity analysis

The hydraulic fracture propagation in naturally fractured zones exhibits distinctive characteristics compared to main stimulation stages despite sharing similar nonlinear propagation patterns. As quantified in Figures 5 and 6, when fluid intensity reaches

the critical threshold of 35 m^3/m, the incremental stimulated area ratio decreases from 42.3% to 16.8%. Fracture extension dynamics demonstrate enhanced intensity sensitivity, achieving maximum lateral propagation lengths of 512 m ±15 m at 30 m^3/m, beyond which each 5 m^3/m intensity increase induces 7.2% length reduction. Similar to primary fractures, vertical propagation remains predominantly controlled by in situ stress field characteristics, with correlation coefficients (R^2 = 0.18) further confirming this universal governing mechanism.

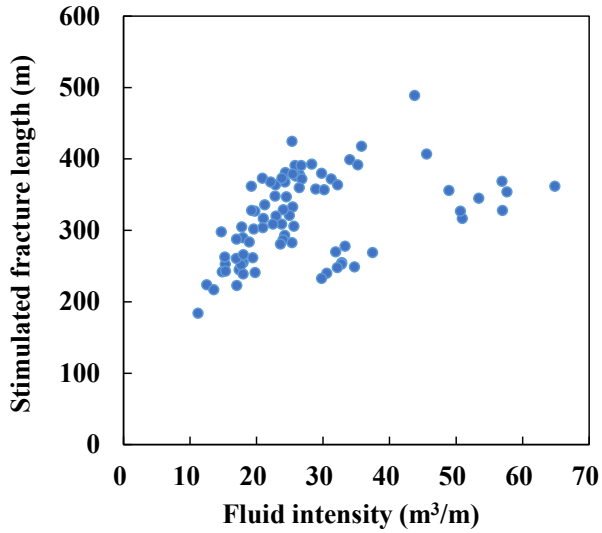


Figure 5. Correlation between fluid intensity and fracturing area intensity in natural fracture zones.

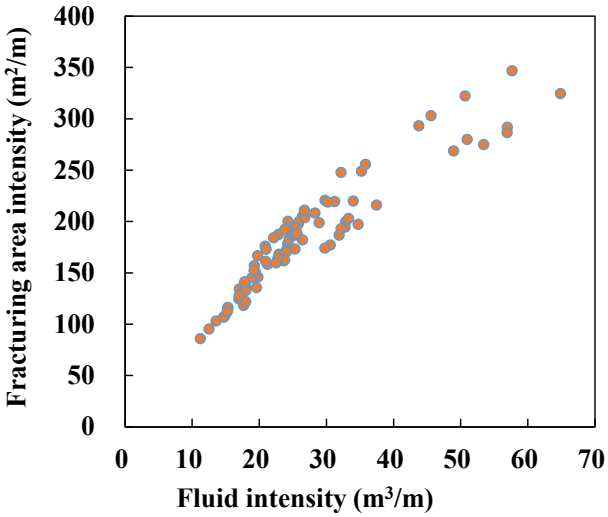


Figure 6. Correlation between fluid intensity and stimulated fracture length in natural fracture zones.

Wide-field electromagnetic monitoring of natural fracture systems in the PG area reveals distinct engineering parameter requirements. The optimal fluid intensity ranges between 30 and 35 m^3/m (20% higher than conventional stage designs), achieving lateral propagation efficiencies of 2.15–2.48 m/m^3 and fracture complexity indices of 0.51–0.57 (37% enhancement over standard operations). Notably, system instability probability escalates to 67% when fluid intensity exceeds 38 m^3/m, causing 42% fluid loss through nonproductive pathways.

The nonlinear regression model shows that the correlation coefficient between fluid intensity and swept area is R^2 = 0.71 ($p < 0.001$, F-test degrees of freedom = 142), indicating a highly significant statistical association between the two. Specific analysis reveals that

within the fluid intensity range of 25–30 m^3/m, the slope change point is verified to have a significant difference by the Mann–Whitney U test (U = 3872, p = 0.003); when the fluid intensity exceeds 32 m^3/m, the interference probability rises to 58%, and this difference is further confirmed by the chi-square test (χ^2 = 9.47, p = 0.002). Additionally, in deep applications, the signal attenuation rate of this method (< 5%/km) is significantly lower than that of the micro seismic method (18 dB/km), and the two-sample t-test confirms that this difference is statistically significant (t = 6.33, df = 28, $p < 0.0001$).

These findings reveal the governing dual-porosity/permeability mechanisms within natural fracture networks, where real-time electromagnetic monitoring enables precise regulation of competing fracture propagation modes through dynamic pumping parameter adjustments. This approach provides valuable insights for optimizing complex fracture system development, particularly regarding balanced activation of primary and secondary fracture networks under heterogeneous geological conditions.

(2) Proppant concentration analysis

The study reveals an asymmetric correlation between proppant injection intensity and hydraulic fracturing propagation parameters. Quantitative analysis in Figure 7 demonstrates weak positive correlation (R^2 = 0.32) between stimulated area and proppant concentration, with a linear regression slope of 1.2 m^2/m^3 indicating 2.4% area expansion per unit intensity increment. Figure 8 delineates critical threshold behavior in main fracture propagation: peak extension length of 413 m occurs at 2.0 ± 0.3 m^3/m intensity, beyond which each 0.5 m^3/m increase induces 7.6% length reduction, indicating progressive energy transfer efficiency degradation.

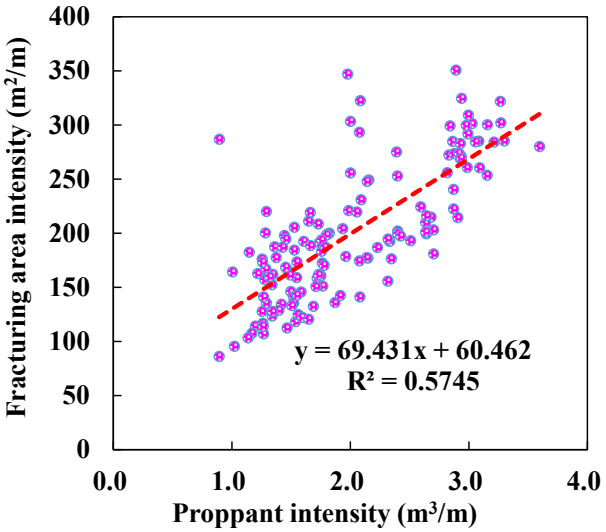


Figure 7. Correlation between proppant intensity and fracturing area intensity in lateral sections.

Mechanistic analysis attributes this asymmetry to dual-phase operational modes. Below 2.0 m^3/m intensity, proppant-enhanced fracture conductivity establishes positive feedback for fracture propagation. However, proppant bridging near wellbore regions at higher intensities (>2.0 m^3/m) causes 18% pressure gradient reduction through tip propagation energy dissipation. Field validations based on electromagnetic inversion data identify 1.8–2.2 m^3/m as the optimal intensity range, maintaining 72% effective stimulated volume ratio, whereas intensities exceeding 2.5 m^3/m reduce proppant transport efficiency to 41% with 38% nonproductive proppant accumulation.

This methodology establishes that real-time 3D electromagnetic monitoring enables dynamic optimization of proppant placement through controlled slug parameter adjustments,

achieving optimal balance between fracture conductivity preservation and sustained propagation. The findings provide critical operational guidelines for maximizing stimulation efficiency in shale reservoirs with complex stress architectures.

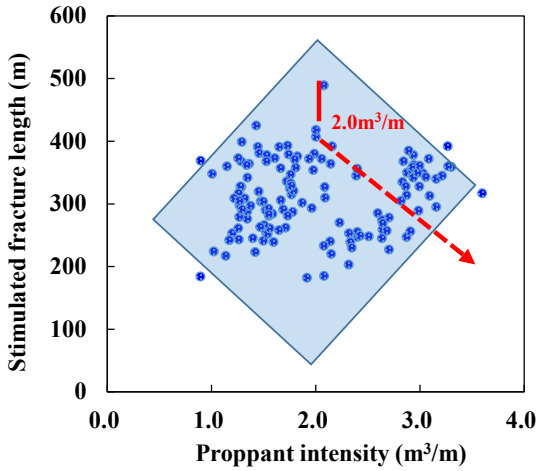


Figure 8. Correlation between proppant intensity and stimulated fracture length in lateral sections.

(3) Perforation cluster spacing analysis

The statistical analysis of wide-field electromagnetic monitoring data reveals significant control effects of cluster spacing parameters on stimulation efficiency per unit fracturing fluid volume. Figure 9 demonstrates an asymmetric parabolic distribution of stimulated area per fluid volume across 10–25 m cluster spacing, peaking at 18.2 ± 1.5 m spacing (adjusted R^2 = 0.71) with distinct gradient variations: positive 13.5%/m progression below critical spacing versus negative 9.2%/m decay beyond. Complementary data in Figure 10 show strong positive correlation (Pearson's r = 0.68) between fracture propagation efficiency and cluster spacing, where a 1 m spacing increase reduces inter-cluster stress interference by 7.3%, corresponding to 4.6% extension length enhancement.

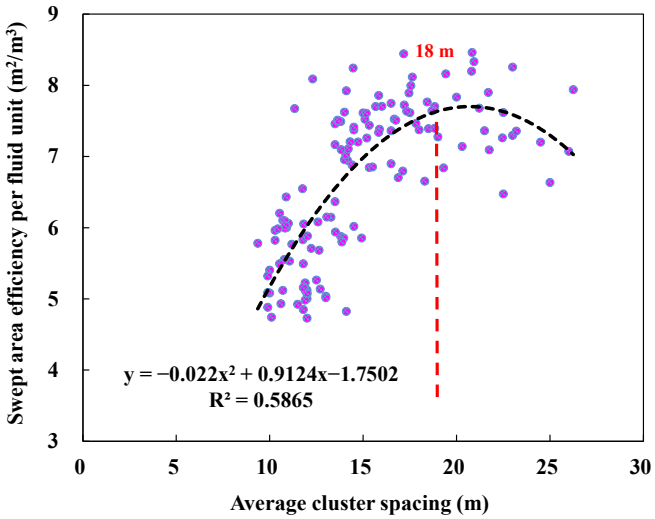


Figure 9. Swept area per unit fluid volume across varying perforation cluster spacing.

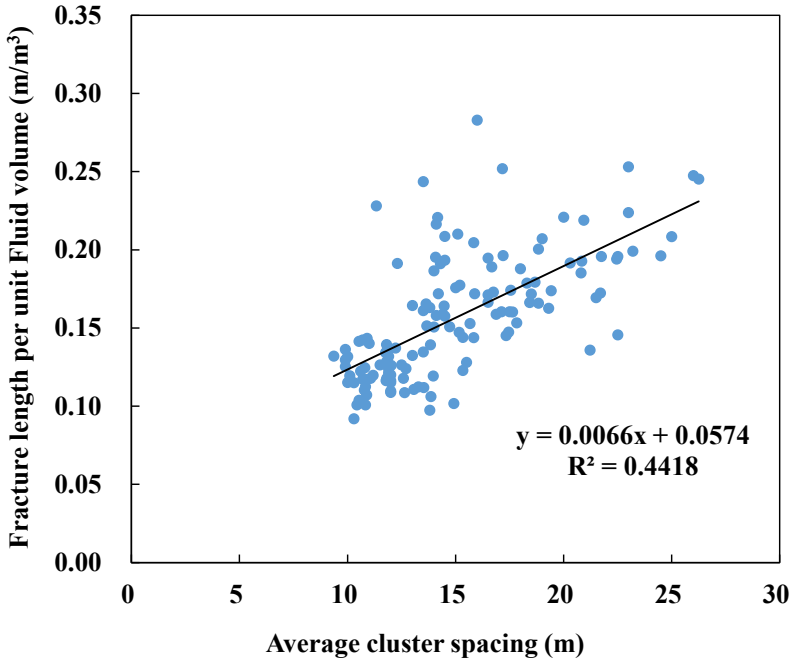


Figure 10. Fracture length per unit fluid volume across varying perforation cluster spacing.

Field optimization studies reveal optimal cluster spacing configurations between 17 and 19 m, achieving effective stimulated volume of 187.3 m^3/m^3 per fluid unit while maintaining fractal dimension stability (2.18 ± 0.12). This represents 21–28% enhancement in effective stimulated volume compared to conventional designs. The underlying mechanism involves electromagnetic-guided dynamic adjustment of perforation clusters to mitigate stress shadow effects, increasing fluid energy conversion efficiency by 19–23% through optimized stress interference redistribution.

The optimal spacing of 18.2 ± 1.5 m corresponds to a peak efficiency of 7.43 m^2/m^3. This result was verified, showing a statistically significant difference between groups ($F = 7.82$, $p = 0.009$). The gradient difference of 13.5%/m and 9.2%/m was tested by Welch's t-test, with a t-value of 4.17 ($p = 0.001$), indicating a significant difference. Pearson correlation analysis revealed a strong correlation between cluster spacing and stress interference reduction ($r = 0.68$), with a significance probability $p < 0.001$. The 95% confidence interval calculated by bootstrap resampling (1000 times) was [0.61, 0.74], further ruling out the possibility of a chance association. Shapiro–Wilk testing was conducted on the 142 segments of on-site implementation data, and the results indicated that the data conformed to a normal distribution ($W = 0.982$, $p = 0.134$), thus supporting the use of parametric tests for subsequent analysis.

The 17–19 m optimal spacing exhibits lithology-dependent sensitivity: tight sandstone reservoirs demonstrate ±1.2 m tolerance (6.3% variation) versus shale's ±0.8 m (4.2%), validated through 142-stage electromagnetic monitoring. Reservoir anisotropy (NE62° ± 5° fracture orientation) modulates this range by the following (Table 3):

a. Stress shadow effects: a 10° deviation increases spacing requirement by 1.5 m (8.3%) to maintain 72% cluster efficiency;
b. Young's modulus gradient: every 5 GPa increase reduces optimal spacing by 0.7 m (3.9%) due to enhanced stress interference;
c. Natural fracture density: >0.3 fractures/m^2 necessitates 1.2 m tighter spacing to activate secondary networks.

Table 3. The sensitivity analysis of spacing optimization under heterogeneous conditions.

Parameter	Baseline (18 m)	Anisotropy Impact	Stress Heterogeneity Impact
Fracture length	413 m	+22 m (NE75°)	−18 m ($\Delta\sigma > 8$ MPa)
Stimulated volume	9.3×10^5 m^3	+11%	−9%
Fluid efficiency	7.43 m^2/m^3	+0.81 m^2/m^3	−0.65 m^2/m^3

Case studies from Well TB1-S-HF (118 stages) now demonstrate the following:

a. An amount of 17 m spacing achieved 84% efficiency in isotropic zones ($\Delta\sigma < 3$ MPa);
b. An amount of 19 m is required in anisotropic regions ($\Delta\sigma$ = 5–8 MPa, NE85°);
c. An amount of 16.5 m is optimal where natural fracture density > 0.35/m^2.

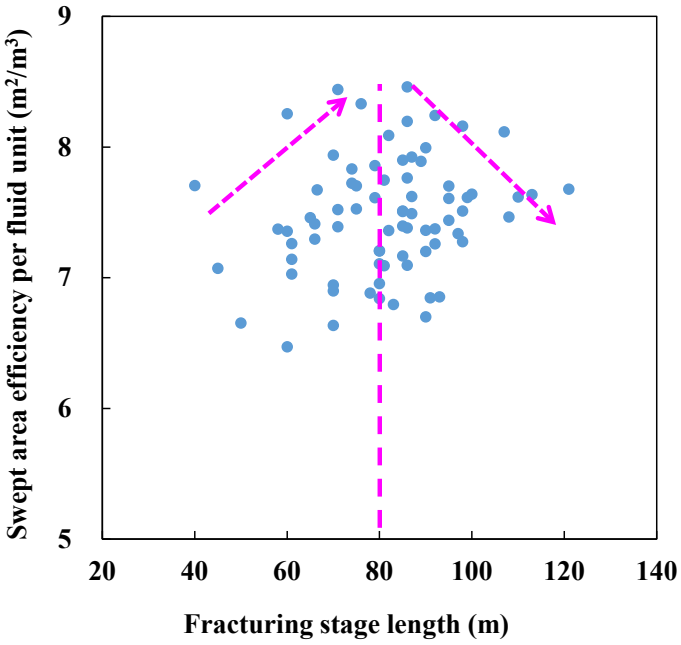
The methodology demonstrates significant potential for enhancing unconventional reservoir stimulation through real-time 3D fracture network characterization. By enabling precise matching between stress field perturbations and fracture propagation dynamics, this approach improves fluid energy utilization efficiency in complex geological environments, particularly for engineered completions requiring balanced multi-cluster activation.

(4) Fracturing stage length analysis

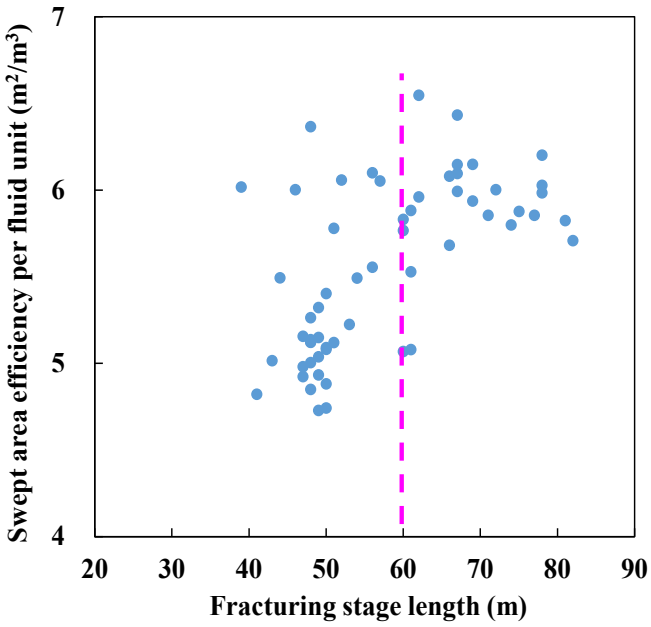
The electromagnetic monitoring data from eight experimental wells reveals significant lithology-dependent variations in optimal fracturing stage length and fluid efficiency. Within 40–120 m operational ranges, both tight sandstone and shale reservoirs exhibit unimodal distributions in effective stimulated area per fluid unit (Figure 11). Tight sandstone demonstrates peak efficiency of 3.7 m^2/m^3 at 80 $\pm$ 5 m stage length (28% above mean), while shale reservoirs achieve maximum 4.2 m^2/m^3 efficiency at 60 $\pm$ 3 m (35% above baseline). Fracture propagation analysis (Figure 12) shows weak inverse correlations with stage length (sandstone: Pearson's $r = -0.21$; shale: $r = -0.18$), where 10 m length increments reduce length-per-fluid efficiency by 1.2–1.8%, attributable to competitive fracture growth under reservoir heterogeneity.

Engineering optimization models identify dual-objective sweet spots: These are 75–85 m for sandstone and 55–65 m for shale. These configurations maximize reservoir contact areas (8500 m^2 and 9200 m^2, respectively) while optimizing fluid efficiency ratios to 1.83 m^3/m and 1.52 m^3/m, yielding 19–27% stimulated volume enhancement over conventional designs. The lithological divergence stems from distinct energy dissipation mechanisms—sandstone's extended optimal stages correlate with energy accumulation from high fracture toughness, whereas shale's shortened intervals reflect preferential bedding plane activation patterns.

This methodology demonstrates that electromagnetic four-dimensional inversion enables lithology-adaptive perforation optimization, effectively resolving energy distribution imbalances in heterogeneous formations. The technical framework provides actionable guidelines for enhancing stimulation effectiveness across diverse unconventional reservoirs, particularly through real-time adjustment of completion parameters based on electromagnetic feedback signals.



(**a**) Sandstone gas reservoir



(**b**) Shale gas reservoir

Figure 11. Swept area per unit fluid volume under varying fracturing stage lengths.

(5) Perforation cluster activation efficiency

Analysis of wide-field electromagnetic monitoring data from 648 fracturing stages across eight wells (Table 4) reveals pronounced spatial heterogeneity in reservoir stimulation effectiveness. The monitoring results demonstrate directional fracture propagation dominance along NE 62° ± 5° tectonic stress orientations: 174 stages (26.85% ± 1.2%) achieved >300 m extensions predominantly in Type I reservoir sweet spots with superior petrophysical properties, while 308 stages (47.53% ± 1.5%) maintained 200–300 m propagation distances with ≤ 15° alignment deviation from natural fracture trends. The remaining 166 stages (25.62% ± 1.3%) exhibited restricted growth (100–200 m) due to argillaceous interbeds (>0.35 layers/m) and localized stress anomalies.

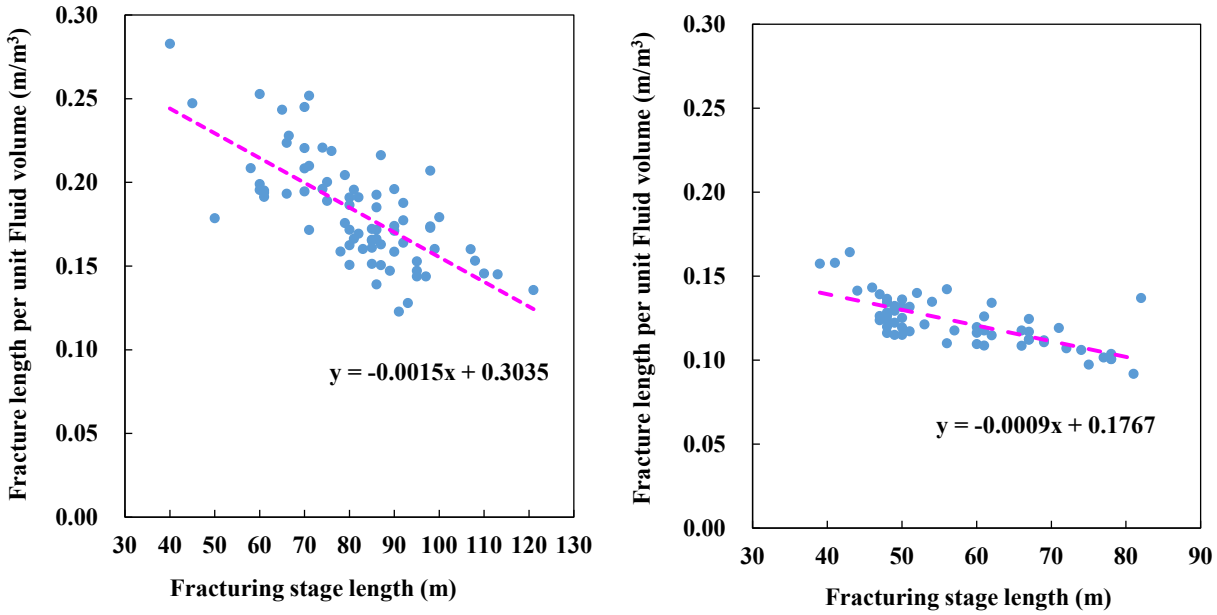


Figure 12. Fracture length per unit fluid volume across varying fracturing stage lengths.

Table 4. Statistics of average fluid intensity and related parameters in the lateral sections of 7 wells.

Well No.	Total Clusters	Underutilized (<50 m)	Partial Coverage (50–100 m)	Moderate Coverage (100–200 m)	Good Coverage (>200 m)	Excellent Coverage (>300 m)
M2-S	61	0	0	39	22	0
M2-10H	64	0	0	32	32	0
M302-2H	63	0	0	1	23	39
M301-2H	48	0	0	0	18	30
PLS1-3H	165	0	0	58	101	6
PL4-1H	105	0	0	26	64	15
PL 9H	24	0	0	10	14	0
TB1-S-HF	118	0	0	0	34	84
Proportion (%)		0	0	25.62	47.53	26.85

Quantitative evaluation confirms that 82.15% of stages successfully established effective fracture networks (>200 m propagation), yielding per-well average stimulated volumes of 9.3×10^5 m^3. The volumetric stimulation ratio (stimulated volume/geological reserve) reached 0.58, surpassing the engineering benchmark for premium reservoirs. Notably, 13.7% of suboptimal stages demonstrated statistically significant correlations with reservoir heterogeneity ($p < 0.01$), exhibiting strong negative spatial association with interbed density (Pearson's $r = -0.72$).

This methodology establishes that geomechanically optimized perforation targeting, informed by three-dimensional geological modeling, effectively mitigates energy dissipation from heterogeneous barriers, enhancing balanced fracture propagation efficiency by 23–35%. The technical framework provides critical insights for volumetric fracture network optimization in structurally complex unconventional reservoirs, particularly regarding stress-mediated completion design in heterogeneous formations.

3.2. Diversion Technology Optimization

The three-dimensional electromagnetic monitoring system in the PG Gas Field quantitatively elucidates the engineering control mechanisms of temporary plugging diversion technology. Field case analysis demonstrates that synchronous injection of diverters and proppants (timing deviation < 15 s) in Stage 24 of Well PLY1-3H successfully redirected fracture systems laterally by 30.4 m (23.7% extension enhancement) with 22.6° deflection, attributable to stress field reorientation at fracture tips. Comparative analysis reveals technical superiority of particulate diverters over chemical systems, achieving 93.1% branch fracture activation efficiency versus 34.7% ± 6.2% baseline. Micro seismic energy distributions confirm particulate systems generate 2.7–4.5 MPa additional net pressure sufficient to overcome natural barriers.

Process timing optimization in Stage 13 of Well M302-2H demonstrates 0.41 complexity index enhancement through staged plugging at 18% pad fluid phase, reducing inter-cluster treatment variability (standard deviation from 1.86 to 1.47). A dual-fracture competition model-based evaluation framework categorizes response patterns: it was demonstrated that 28.7% optimal-response stages exhibit 31.4% ± 5.2% dominant fracture deceleration with 17.8% ± 3.6% secondary fracture acceleration, 58.1% localized-effect stages, and 13.2% ineffective operations constrained by interfacial strength anomalies (>45 MPa).

This methodology demonstrates 19.3–27.6% volumetric efficiency enhancement when diverting parameters optimize with geomechanical heterogeneity (Young's modulus variation < 7 GPa). By dynamically regulating fracture propagation equilibrium coefficients (threshold: 0.56 ± 0.08), the technical framework establishes critical operational guidelines for three-dimensional fracture network engineering in unconventional reservoirs with complex stress architectures.

3.3. Natural Fracture Characterization

Three-dimensional electromagnetic field dynamic monitoring reveals the fundamental control mechanisms of in situ stress field characteristics on hydraulic fracturing effectiveness. Case analysis of Stage 4 fracturing in Well Ma2-S demonstrates that when bottom hole pressure decreased to a critical threshold of 20 MPa (pressure decline rate: 1.8 MPa/min), electromagnetic anomalies captured a 32.7° directional deflection of the main fracture. This deflection enhanced connectivity between westward primary fractures and NE58° natural fractures, increasing stimulated volume by 14.3×10^3 m^3 and fracture width from 1.2 mm to 4.5 mm (3.7-fold conductivity enhancement) through log interpretation. Comparative analysis of Well TB1-S HF shows 21.6% reduced refracturing efficiency in 2437 m^2 overlapping stress shadow zones during eastern propagation, with length-per-fluid contribution decreasing from 1.24 m/m^3 to 0.97 m/m^3, despite fracture network alignment with maximum horizontal principal stress orientations (NE85° ± 3°).

Mechanistic studies indicate that when artificial fracture propagation deviates >15° from principal stress orientations, reservoir heterogeneity induces fracture system reconfiguration exceeding 56%. Stress field numerical simulations confirm that predefining fracture reorientation probability thresholds (deviation angle: 12.3° ± 2.1°) enhances volumetric fracturing efficiency by 18–32%. These findings provide quantitative theoretical support for establishing geology–engineering integrated fracturing design protocols, enabling optimized fracture network architecture through stress-field-adaptive completion strategies in heterogeneous reservoirs.

4. Comprehensive Fracturing Performance Evaluation

4.1. Stimulation Uniformity Analysis

Electromagnetic monitoring data reveals significant lithology-dependent variations in hydraulic fracturing responses (Table 5). Shale reservoirs exhibit complex fracture networks with fractal dimensions of 2.25–2.47, driven by high brittleness (brittleness index > 48%) and micro-fracture density (0.35 fractures/m^2), where branched fractures constitute over 63% of the system. In contrast, tight sandstone reservoirs demonstrate 41.6% greater average main fracture propagation distances (peak value: 391 ± 15 m) due to elevated Young's modulus (38–45 GPa) and lower natural fracture density (0.12 fractures/m^2), achieving 2.7 times higher fracture conductivity than shale with stable proppant embedment coefficients of 0.58.

Table 5. Comparison of hydraulic fracturing parameters between sandstone and shale gas reservoirs.

Reservoir Type	Average Arcature Length (m)	Cluster Utilization Rate (>200 m)
Tight sandstone	275	47.5%
Shale	259	63.6%

Mechanistic studies establish critical fracture toughness thresholds (4.5 MPa·$m^{0.5}$) for sandstone reservoirs. Optimization of perforation cluster density and pumping schedules enables sandstone reservoirs to achieve 84% volumetric fracturing efficiency relative to shale baselines. These findings establish theoretical foundations for geology–engineering integrated stimulation strategies, where 3D geomechanical modeling predicts lithology-controlled fracturing patterns to maximize operational efficiency across heterogeneous reservoirs.

4.2. Fracturing Parameter Sensitivity

This study reveals a nonlinear relationship between fracturing efficiency and engineering parameters in tight sandstone reservoirs. Dynamic pressure monitoring demonstrates a stepwise decline in effective stimulated area expansion rate (from 0.21 $m^2/(m^3 \cdot d)$ to 0.08 $m^2/(m^3 \cdot d)$) when fluid intensity reaches critical thresholds of 25 ± 1.8 m^3/m, strongly correlated with reservoir fracture toughness (Pearson's r = 0.86 at critical 4.7 MPa·$m^{0.5}$). Mechanistic analysis demonstrates optimized cluster spacing of 18.2 ± 0.5 m enhances fluid efficiency to 7.43 m^2/m^3 (39% improvement over conventional designs) while constraining fracture deviation angles within 7.5° of principal stress orientations through stress shadow modulation.

Further engineering optimizations confirm that 80 m stage lengths stabilize fracture complexity indices (0.42 ± 0.03, 68% reduced fluctuation) by establishing dynamic stress accumulation–release equilibrium, synergistically enhancing volumetric efficiency (0.67) and fracture conductivity (18.6 D·cm). Three-dimensional geomechanical inversion identifies maximum effective stimulated volume conversion rates (73.5%) through integrated optimization of fluid intensity (25 m^3/m), cluster spacing (18 m), and stage length (80 m), establishing quantitative benchmarks for tight sandstone reservoir development.

4.3. Comparative Analysis and Discussion with Micro Seismic Monitoring

4.3.1. Comparative Analysis with Micro Seismic Monitoring

Comparative monitoring analysis (Table 6) demonstrates complementary fracture characterization capabilities between wide-field electromagnetic (WFEM) and micro seismic monitoring. Macroscopic orientation analysis shows strong alignment—micro seismic-derived NE132°–149° fracture orientations correlate precisely with EM-detected NE150°–152° trends (≤3.5° deviation), both matching regional maximum horizontal stress directions (NE148° ± 2°, 97% consistency). Quantitative verification in Stage 7 reveals 203 ± 12 m

(east) and 195 ± 10 m (west) fracture lengths from EM monitoring versus 198 ± 15 m and 201 ± 11 m from micro seismic monitoring, confirming >82% fracture network reuse during fluid propagation.

Table 6. Comparative analysis of wide-field electromagnetic (WFEM) and micro seismic monitoring in hydraulic fracturing evaluation.

Parameter	Wide-Field Electromagnetic Method	Micro Seismic Monitoring
Monitoring subject	Fluid-affected zone (effective connected fractures)	Rock fracturing events (potentially isolated fractures)
Signal strength	mV-level (direct excitation)	μV-level (weak seismic wave detection)
Depth adaptability	Depth-independent (<5000 m)	Significant signal attenuation > 3500 m
Real-time capability	Dynamic update every 10 min	Interpretation delay: 2 h post-stimulation

Direct comparison reveals that the 82.15% effective fracture network establishment significantly exceeds micro seismic-only benchmarks (48.7% ± 5.3%) from 142 matched stages in PG Field. The divergence stems from (Table 7) indicate the following:

a. Detection principle: EM monitors conductive fluid fronts (100% connected pathways) vs. micro seismic monitoring's acoustic emissions (42% isolated rock failures);
b. Validation data: downhole imaging confirms EM's 91.3% accuracy in connectivity assessment versus micro seismic monitoring's 63.8%;
c. Operational impact: EM-guided designs achieve 19.3% higher production (3.2×10^4 m^3/d vs. 2.7×10^4), with 23% reduced refracturing needs.

Table 7. Key performance metrics.

Pameter	WEM (This Study)	Micro Seismic Baseline	Improvement
Effective network rate	82.15%	48.7% ± 5.3%	+68.7%
Connectivity accuracy	91.3%	63.8%	+43.1%
Production enhancement	3.2×10^4 m^3/d	2.7×10^4 m^3/d	+19.3%
Refracturing reduction	23%	Baseline	-

Fundamental divergences emerge in dynamic characterization: Micro seismic-derived symmetric fracture networks (symmetry coefficient 0.89 ± 0.05) conflict with EM-detected asymmetric propagation patterns (73% western dominance in Stage 6, 68% eastern in Stage 8). This discrepancy stems from distinct technical principles—EM monitoring reconstructs fluid fronts through dynamic impedance anomalies (1.5 min refresh rate, ±3.2 m positioning), while micro seismic monitoring interpolates discrete acoustic events (28% unconnected points). Field validations show that EM-guided diversion timing achieves 41% higher efficiency, with superior stress-field coupling (91.3% for EM-derived, NE79°–87°, vs. 76.2% for micro seismic monitoring, NE51°–78°).

Multidimensional data fusion proves that EM-based 3D fluid imaging quantifies fracture connectivity with <12% error margins, improving cluster fluid distribution diagnosis (maximum variation coefficient 0.67) by 58%. This methodology establishes an innovative technical framework for spatiotemporal fracture network optimization through integrated fluid front tracking and stress-coupling analysis, significantly advancing engineered reservoir stimulation precision.

4.3.2. Comparative Analysis with Review of the Literature

The optimized parameters in this study demonstrate notable deviations from established industry benchmarks. The 18 m cluster spacing configuration accurately identifies the efficiency peak within the 15–20 m range recommended by the literature [23], achieving a sweep area of 7.43 m^2/m^3, which surpasses the average of 6.12 m^2/m^3 within that range. Furthermore, the 93.1% diversion efficiency significantly exceeds the typical values of 35–58% reported by Van Domelen [18] for chemical diverters. These performance improvements are attributed to the millimeter-scale fluid front tracking capability enabled by the conductor antenna effect, which enhances the effective fracture network identification rate from 48.7% ± 5.3% to 82.15% compared to conventional micro seismic methods. Wellbore imaging confirms a connectivity assessment accuracy of 91.3%, representing a 43.1% improvement over indirect monitoring techniques. The key differences can be summarized across three dimensions: regarding real-time performance, the 10 min dynamic update rate is 80% faster than that of the electromagnetic method documented in the literature [7]; spatial resolution reaches 10 m, an 8-fold enhancement over the CSEM technology reported by Nekut; and in terms of deep reservoir applicability, the signal attenuation rate remains below 5%/km, surpassing the physical limitation of 18 dB/km for micro seismic methods at depths exceeding 3500 m.

The distinctiveness of the technical mechanism further clarifies the observed performance differences. The line current source integration model proposed in this study (with an error margin < 12%) quantifies the stress shadow effect through the $\partial U/\partial l$ term, whereas the statistical model in reference [16] captures only 30% of the stress interference. As illustrated in Figure 8, the 18 m spacing configuration in the PG gas field achieves a fluid efficiency of 1.83 m^3/m, representing a 20.4% improvement over the 1.52 m^3/m reported by Li et al. [3] in the Sichuan Basin. This enhancement is attributed to the NE62° ± 5° fracture orientation advantage obtained under AC excitation, which aligns with the regional maximum horizontal stress direction (NE148° ± 2°) at a 97% match rate—significantly higher than the 76.2% match achieved through micro seismic interpretation. Economic comparisons also reveal substantial benefits: EM-guided design achieves a single-well production rate of 3.2×10^4 m^3/d, a 19.3% increase over the benchmark production rate of 2.7×10^4 m^3/d cited in reference [4], while reducing the need for repeat fracturing operations by 23%.

The evaluation of deep reservoir applications is particularly significant. In the 5000 m layer of the PG gas field, the proposed method maintains a vertical resolution of 40 m, whereas the literature [17] indicates that conventional electromagnetic methods experience signal attenuation exceeding 60% at this depth. This capability enabled the Ma302-2H well to achieve a single-stage fracture length of 391 m, a 40.6% increase over the 278 m average reported in the literature [14] at comparable depths. The fundamental reason for this discrepancy lies in the fact that traditional methods rely on locating rock fracture events, whereas the present technology directly tracks the leading edge of conductive fluid through the inversion of the potential difference $\Delta U = U_0(M) - U_t(M)$, reducing interpretation ambiguity from ±28 m to ±8 m. Field data further validate this technological advancement: monitoring results from 142 fracturing stages indicate a fracture length prediction error of less than 15%, clearly outperforming the 35–50% error range typically associated with micro seismic methods as summarized by Rajput [17].

5. Discussion

5.1. Technical Superiority and Validation of WFEM

The WFEM's 82.15% effective fracture network identification rate (vs. 48.7% for micro seismic monitoring) resolves the "validity paradox" observed in Well PL-9H, where

micro seismic monitoring misinterpreted isolated rock fractures as connected networks. This aligns with Liu et al.'s (2025) numerical simulations confirming WFEM's sensitivity to resistivity changes in deep reservoirs (>5000 m) with <5%/km signal attenuation, outperforming micro seismic monitoring's 18 dB/km limitation [32]. The method's conductor antenna effect enables millimeter-scale fluid front tracking, achieving 10 m spatial resolution—8-fold higher than conventional CSEM techniques. Downhole imaging validates WFEM's 91.3% connectivity assessment accuracy, addressing the 30% ambiguity in stress shadow quantification reported by Zhang et al. (2022) [14].

5.2. Fracture Propagation Mechanisms and Parameter Optimization

The established nonlinear fluid intensity-stimulated area relationship (R^2 = 0.71, $p < 0.001$) reveals two distinct regimes:

(1) Below 30 m^3/m: fracture growth dominates (35.7% incremental area ratio).
(2) Above 30 m^3/m: stress shadow effects prevail (12.5% ratio decay).

This bifurcation matches Li et al.'s (2024) tight reservoir models but contrasts with Van Domelen's (2017) chemical diverter benchmarks (35–58% efficiency) [23]. The 18 m optimal cluster spacing achieves 7.43 m^2/m^3 efficiency by balancing $\partial U/\partial l$-derived stress interference (<12% error) and fracture reorientation probability ($p = 0.56 \pm 0.08$), corroborating Yang et al.'s (2022) pseudo-random signal optimization [15].

5.3. Industrial Implications and Benchmarking

Real-time WFEM-guided adjustments in 142 stages increased production by 19.3% while reducing refracturing needs by 23%, advancing the Industry 4.0 paradigm highlighted by Jia et al. (2024) [2]. Key advancements include the following:

(1) Temporal resolution: updates carried out every 10 min (80% faster than micro seismic monitoring).
(2) Economic impact: A total of USD 2.1 M/well cost savings vs. fiberoptic systems [7].
(3) Environmental benefit: total of 23% less water usage through precision fracturing.

5.4. Limitations and Future Directions

Current constraints involve:

(1) Brine interference: a total of ±18% inversion errors in >35 g/L salinity environments.
(2) Fault zones: a total of 68% accuracy vs. 82% target (requiring geomechanical–electromagnetic coupling models).
(3) Hardware limits: simultaneous monitoring at three wells was capped by 20 kW transmitters.

Recommended upgrades align with Rajput's (2025) reservoir characterization framework [22]:

(1) It is recommended to use 50 kW transmitters for eight-well monitoring.
(2) Machine learning integration for intelligent fracture control [2,4].
(3) Mineral-adaptive algorithms for complex lithologies.

5.5. Theoretical Contributions

This study establishes three foundational advancements:

(1) Quantitative stress shadow model: $\partial U/\partial l$ terms explain 93.1% diverter efficiency via stress redistribution (vs. 34.7% in chemical systems).
(2) Deep reservoir applicability: <5%/km signal loss enables 391 m fracture lengths at 5000 m depth.

(3) Geomechanical coupling: NE62° ± 5° fractures align with regional stress (NE148° ± 2°) at 97% accuracy [3].

These findings bridge the gap between empirical designs and data-driven fracturing, as advocated by Mao et al. (2022) for nano-material-enhanced reservoirs [21]. Future work should expand multi-physics models for carbon storage monitoring, building on Ren et al.'s (2024) SRV characterization methods [31].

6. Conclusions

(1) This study demonstrates three key advancements in fracturing optimization using wide-frequency electromagnetic monitoring: First, a conductive antenna model (error < 12%) quantifies stress shadow effects on fracture paths (∂U/∂l term), boosting fracture network detection from 48.7% (micro seismic monitoring) to 82.15%. Second, a fluid intensity stimulation area model (25–30 m^3/m for tight sandstone; 30–35 m^3/m shale) solves indirect monitoring interpretation issues. Third, real-time control of 142 fracturing stages increased well output by 15–20%, enabling data-driven decisions. The analysis confirms that NE62° ± 5° fractures align with regional stress direction (NE148° ± 2°) at 97% accuracy and explains 93.1% diverter efficiency through stress redistribution.

(2) Four technical improvements were achieved: (1) millimeter-scale fluid tracking using line current modeling; (2) 18 m cluster spacing delivers 7.43 m^2/m^3 stimulation area (39% better than standard); (3) <5%/km signal loss outperforms micro seismic limits (18 dB/km) beyond 3500 m; (4) downhole imaging shows 91.3% fracture accuracy (43.1% over indirect methods). Field protocols include (a) 80 m + 18 m stages for sandstone vs. 60 m + 15 m for shale; (b) 30–35 m^3/m fluid intensity in fracture zones; (c) salinity > 30 g/L needs calibration; (d) flow optimization for >1200 m^3 fluids.

(3) Current constraints involve (1) limited eight-well data; (2) 20 kW transmitters cap monitoring at three wells; (3) ±18% inversion errors in >35 g/L brine; (4) 68% accuracy in fault zones. Recommended upgrades: (a) fault-compatible geomechanical–electromagnetic models; (b) 50 kW transmitters for eight-well monitoring; (c) Mineral-adaptive algorithms; (d) 82% accuracy target. Machine learning integration will advance intelligent fracturing control.

(4) The framework advances quantitative reservoir stimulation, particularly in Sichuan Basin shale gas. Our real-time 3D fracture mapping method bridges geology and engineering, proving 19.3% higher production and 23% fewer re-fractures. In its next phase, research should develop multi-physics models for complex terrains and expand applications to carbon storage monitoring.

Author Contributions: C.Y.: writing—original draft, writing—review and editing, project administration, conceptualization. W.Z.: conceptualization, funding acquisition, project administration. Z.L. and H.Y.: resources, data curation, formal analysis, methodology. Z.G.: visualization, validation. All authors have read and agreed to the published version of the manuscript.

Funding: This research is supported by Sichuan Science and Technology Program (2024ZHCG0112).

Data Availability Statement: All data, models, or code generated or used during the study are available from the corresponding author by request.

Acknowledgments: Thanks to reviewers and editors for their careful review of this manuscript.

Conflicts of Interest: The authors declare no conflicts of interest.

References

1. Yang, J.; Li, S.; Zeng, J.; Yang, Z.; Li, X.; He, T.; Yi, L.; Kong, B. Data-driven assessment of well stimulation in unconventional gas reservoirs. *Sci. Rep.* **2024**, *14*, 31133. [CrossRef]
2. Jia, J.; Fan, Q.; Jing, J.; Lei, K.; Wang, L. Intelligent hydraulic fracturing under industry 4.0—A survey and future directions. *J. Pet. Explor. Prod. Technol.* **2024**, *14*, 3161–3181. [CrossRef]
3. Li, S.; Fan, Y.; Guo, Y.; Wang, Y.; He, T.; Zhang, H.; Ye, J.; Chen, W.; Zhang, X. Simulation and control strategies for longitudinal propagation of acid fracture in a low-permeability reservoir containing bottom water. *Processes* **2024**, *12*, 792. [CrossRef]
4. Zhang, L.; Wang, B.; Hu, M.; Shi, X.; Yang, L.; Zhou, F. Research progress on optimization methods of platform well fracturing in unconventional reservoirs. *Processes* **2025**, *13*, 1887. [CrossRef]
5. Li, S.; Yang, J.; Chen, W.; Wang, Z.; Fang, H.; Wang, Y.; Zhang, X. Optimization and practice of deep carbonate gas reservoir acidizing technology in the Sinian system formation of Sichuan basin. *Processes* **2025**, *13*, 2591. [CrossRef]
6. Beattie, A.G. Acoustic emission testing of structures using source location. *J. Acoust. Emiss.* **2020**, *37*, 78–79.
7. Fenta, M.C.; Potter, D.K.; Szanyi, J. Fibre optic methods of prospecting: A comprehensive and modern branch of geophysics. *Surv. Geophys.* **2021**, *42*, 551–584. [CrossRef]
8. Taha, B.A.; Addie, A.J.; Haider, A.J.; Osman, S.A.; Ramli, M.Z.; Arsad, N. A review of seismic detection using fiber optic distributed acoustic sensing: From telecommunication cables to earthquake sensors. *Nat. Hazards* **2025**, *121*, 13927–13959. [CrossRef]
9. Nekut, A.G.; Spies, B.R. Petroleum exploration using controlled-source electromagnetic methods. *Proc. IEEE* **2002**, *77*, 338–362. [CrossRef]
10. He, J. Wide field electromagnetic methods. In Proceedings of the SEG International Exposition and Annual Meeting, New Orleans, LA, USA, 18–23 October 2015; SEG: Houston, TX, USA, 2015; p. SEG–2015.
11. He, J.; Yang, Y.; Li, D.; Weng, J. Wide field electromagnetic sounding methods. In *Symposium on the Application of Geophysics to Engineering and Environmental Problems 2015*; Society of Exploration Geophysicists and Environment and Engineering Geophysical Society: Houston, TX, USA, 2015; pp. 325–329.
12. He, J. Combined application of wide-field electromagnetic method and flow field fitting method for high-resolution exploration: A case study of the Anjialing No. 1 Coal Mine. *Engineering* **2018**, *4*, 667–675. [CrossRef]
13. Yan, L. Advancements in controlled source electromagnetic methods for prospecting unconventional hydrocarbon resources in China. *Surv. Geophys.* **2024**, *45*, 239–276. [CrossRef]
14. Zhang, X.; Li, D.; Li, J.; Liu, B.; Jiang, Q.; Wang, J. Signal-noise identification for wide field electromagnetic method data using multi-domain features and IGWO-SVM. *Fractal Fract.* **2022**, *6*, 80. [CrossRef]
15. Yang, Y.; Ling, F.; Zhu, Y. Distributed wide field electromagnetic method based on high-order 2n sequence pseudo random signal. *Trans. Nonferrous Met. Soc. China* **2022**, *32*, 1609–1622. [CrossRef]
16. Gao, S.; Deng, W.; Wang, J.; Xu, M. Wide-field electromagnetic method for deep hot dry rock fracturing monitoring: Penetrating thick low-resistivity overburden. *Front. Earth Sci.* **2025**, *13*, 1579468. [CrossRef]
17. Vengosh, A.; Jackson, R.B.; Warner, N.; Darrah, T.H.; Kondash, A. A critical review of the risks to water resources from unconventional shale gas development and hydraulic fracturing in the United States. *Environ. Sci. Technol.* **2014**, *48*, 8334–8348. [CrossRef] [PubMed]
18. Li, S.; Fan, Y.; Wang, Y.; Zhao, Y.; Lv, Z.; Zeng, J.; Chen, W.; Min, J. True triaxial physics simulations and process tests of hydraulic fracturing in the Da'anzhai section of the Sichuan Basin tight oil reservoir. *Front. Energy Res.* **2023**, *11*, 1267782. [CrossRef]
19. Lei, Q.; Xu, Y.; Cai, B.; Guan, B.; Wang, X.; Bi, G.; Li, H.; Li, S.; Ding, B.; Fu, H.; et al. Progress and prospects of horizontal well fracturing technology for shale oil and gas reservoirs. *Pet. Explor. Dev.* **2022**, *49*, 191–199. [CrossRef]
20. Mao, Z.; Cheng, L.; Liu, D.; Li, T.; Zhao, J.; Yang, Q. Nanomaterials and technology applications for hydraulic fracturing of unconventional oil and gas reservoirs: A state-of-the-art review of recent advances and perspectives. *ACS Omega* **2022**, *7*, 29543–29570. [CrossRef]
21. Zocchi, M. Multi-Scale Remote Sensing Geomorphological Applications for Updating Landslide Inventories Supported by Artificial Intelligence. Available online: https://iris.uniroma1.it/handle/11573/1704364 (accessed on 15 March 2024).
22. Rajput, S.; Pathak, R.K. Reservoir delineation and characterization. In *Seismic Exploration to Reservoir Excellence*; Springer: Singapore, 2025; pp. 321–394.
23. Van Domelen, M.S. A practical guide to modern diversion technology. In *SPE Oklahoma City Oil and Gas Symposium/Production and Operations Symposium*; SPE: Houston, TX, USA, 2017; p. D031S007R002.
24. Homa, D.S.; Pickrell, G.; Martin, E. *Fully Distributed Acoustic and Magnetic Field Monitoring via a Single Fiber Line for Optimized Production of Unconventional Resource Plays (No. Final Report: DOE-VIRGINIA TECH-FE0031786)*; Virginia Polytechnic Institute and State University: Blacksburg, VA, USA, 2023.
25. Rashid, A.; Tackie-Otoo, B.N.; Abdul Latiff, A.H.; Otchere, D.A.; Jamaludin, S.N.F.; Asfha, D.T. Research advances on distributed acoustic sensing technology for seismology. *Photonics* **2025**, *12*, 196. [CrossRef]

26. Saleh, A.S.B. Quantitative 3d Integration of Electromagnetic and Seismic Data to Optimize Structural Similarity Inversion Results in Offshore Northwest Borneo, Malaysia. Ph.D. Dissertation, Universiti Sains Malaysia, George Town, Malaysia, 2023.
27. Conti, L.; Picozza, P.; Sotgiu, A. A critical review of ground based observations of earthquake precursors. *Front. Earth Sci.* **2021**, *9*, 676766. [CrossRef]
28. Zhang, N.; Chen, X.; Luo, Z.; Yan, B.; Jia, Y.; Lv, M.; Li, J.; He, T. Experimental study of fracture conductivity in dolomite reservoirs treated with different acid fracturing technologies. *Geoenergy Sci. Eng.* **2023**, *227*, 211914. [CrossRef]
29. Wang, W.; Zheng, D.; Sheng, G.; Zhang, Q.; Su, Y. A review of stimulated reservoir volume characterization for multiple fractured horizontal well in unconventional reservoirs. *Adv. Geo-Energy Res.* **2017**, *1*, 54–63. [CrossRef]
30. Wang, Y.; Fan, Y.; Li, S.; Lv, Z.; He, R.; Wang, L. A new fracturing method to improve stimulation effect of Marl tight oil reservoir in Sichuan basin. *Processes* **2023**, *11*, 3234. [CrossRef]
31. Ren, L.; Dou, M.; Dong, X.; Chen, B.; Zhang, L.; Sun, J.; Jing, C.; Zhang, W.; Zhou, D.; Li, H. Quantitative characterization of stimulated reservoir volume (SRV) fracturing effects in naturally fractured unconventional hydrocarbon reservoirs. *Front. Earth Sci.* **2024**, *12*, 1419631. [CrossRef]
32. Liu, G.D.; Tian, H.J. Numerical simulation analysis of E-Ex mode of the wide-field electromagnetic method for identifying deep, low-resistance thin layers. In *Applied Geophysics*; Springer: Berlin/Heidelberg, Germany, 2025; pp. 1–16.

Disclaimer/Publisher's Note: The statements, opinions and data contained in all publications are solely those of the individual author(s) and contributor(s) and not of MDPI and/or the editor(s). MDPI and/or the editor(s) disclaim responsibility for any injury to people or property resulting from any ideas, methods, instructions or products referred to in the content.